IEEE Robotics and Automation Letters (RA-L) paper, presented at ICRA 2024, Yokohama, Japan. Cite as RA-L paper.

Barry: a high-payload and agile quadruped robot

Giorgio Valsecchi, Nikita Rudin, Lennart Nachtigall, Konrad Mayer, Fabian Tischhauser, Marco Hutter

***Abstract*—This paper introduces Barry, a dynamically balancing quadruped robot optimized for high payload capabilities and efficiency. It presents a new high-torque and low-inertia leg design, which includes custom-built high-efficiency actuators and transparent, sensorless transmissions. The robot's reinforcement learning-based controller is trained to fully leverage the new hardware capabilities to balance and steer the robot. The newly developed controller can manage the non-linearities introduced by the new leg design and handle unmodeled payloads up to 90 kg while operating at high efficiency. The approach's efficacy is demonstrated by a high payload-to-weight ratio verified with multiple tests, with a maximum ratio of 2 on flat terrain. Experiments also demonstrate Barry's power consumption and cost of transport, which converge to a value of 0.7 at 1.4 m/s, regardless of the payload mass.**

***Index Terms*—Legged Robots, Actuation and Joint Mechanisms, Mechanism Design.**

I. Introduction

LEGGED robots have the potential to bring disruptive change in various fields, including industrial, smart cities, and domestic use cases. Although wheeled and tracked platforms are cost-effective and suitable for many tasks, legged robots offer established advantages, being the preferred solution for challenging terrains, unstructured environments, and complex tasks. It is expected that intelligent walking machines will become a part of our daily lives soon.

Significant advances in recent years have demonstrated the viability of walking robots in multiple scenarios. In controlled environments, bipedal robots can demonstrate impressive performances like those of human athletes [1]. A variety of humanoid robots have showcased impressive performances at the DARPA Robotic Challenge [2]. In more hostile environments, legged robots can be successfully employed for complex missions, such as the DARPA Subterranean (SubT) Challenge [3], [4], [5]. From a business perspective, dynamically balancing robots are already commercially available [6], [7], [8] and are starting to be integrated into different applications.

The expectations for what robots can do are constantly growing. However, legged robots are still too weak, slow, inefficient, or fragile to take over tasks that involve heavy payloads, long distances, and environments designed for humans. Legged robots can outperform traditional alternatives only in a minority of applications. Currently, the limitations of robots' capabilities can be attributed to both hardware, which defines the physical boundaries of the performance, and software, which determines how close we can push the robot to its limits.

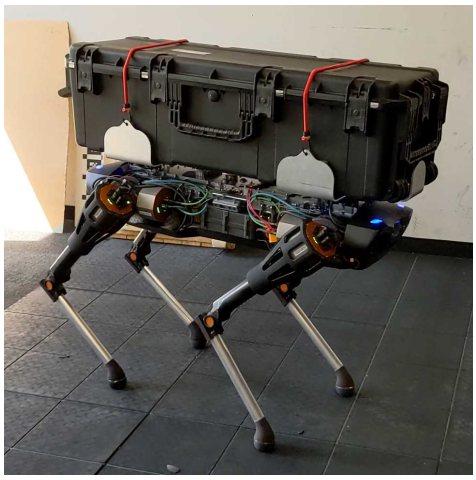

Fig. 1: Barry carrying a box used to contain various payloads and to showcase its transportation capabilities.

Increasing the payload capacity of walking robots would enable new applications, while increased autonomy would allow for longer missions and reduced downtime. Moving things from one place to another requires a lot of physical labor and can cause numerous injuries and accidents. Legged robots have great impact potential in unstructured environments like construction sites, mines, and agricultural fields. Payload transportation is a task that legged robots could address, and it can be captured by hard metrics, making it possible to compare and benchmark different robots.

In this paper, we present Barry, a quadruped robot standing at a height of $1\,\mathrm{m}$ and weighing $48\,\mathrm{kg}$, optimized for payload and cost of transport. Barry shows better performance than published state-of-the-art robots, while maintaining high mobility and dynamic locomotion capabilities. Barry is a research platform designed to improve our understanding of walking robots, push existing technology boundaries, and explore new real-world applications. To properly contextualize the development of Barry, we review the prior art and physical effects dominating the design of legged robots in Section II. In Section III, we introduce Barry's actuation and design. In Section IV, we present the software setup and locomotion control algorithms used. We describe the experimental results and overall system performance in Section V, while Section VI discusses and summarizes the outcomes.

II. State of the Art and Theoretical Limits

Walking robots are complex systems designed to solve a broad range of tasks and integrate auxiliary subsystems. The concept of optimality differs for each use case, and there is no single metric that can capture the entire performance of a walking robot. Therefore, we have summarized the most

Manuscript received: May, 9, 2023; Revised July, 8, 2023; Accepted August, 28, 2023.

This paper was recommended for publication by Editor Abderrahmane Kheddar upon evaluation of the Associate Editor and Reviewers' comments.

This work was supported by ESA Contract Number 4000131516/20/NL/MH/ic.

All the authors are with All authors are with the Robotic Systems Lab (RSL), ETH Zurich, Switzerland. vgiorgio@ethz.ch

Digital Object Identifier (DOI): see top of this page.

IEEE Robotics and Automation Letters (RA-L) paper, presented at ICRA 2024, Yokohama, Japan. Cite as RA-L paper.

IEEE Robotics and Automation Letters (RA-L) paper, presented at ICRA 2024, Yokohama, Japan. Cite as RA-L paper.

relevant figures for dynamically balancing quadrupedal robots developed in the last decades in Tab.I. We have distinguished between the maximum values achieved and those used to compute derived metrics, such as autonomy and cost of transportation (COT). We have also provided comments on details that affect the comparisons between robots.

In 2008, Boston Dynamics' Big Dog [9] and LS3 [13] achieved large payloads and autonomy compatible with real-world applications. This was accomplished using an internal combustion engine (ICE) generator, combined with gasoline as a primary energy source, and hydraulic actuation. Gasoline has very high specific energy, and hydraulic actuation provides the highest force-to-weight ratio amongst actuation principles, particularly at larger scales [22]. However, hydraulic oil leakages [23] and ICE's exhaust gases are hardly reconcilable with indoor applications and humans. Moreover, the achieved COT was high, indicating low efficiency.

Electrically actuated robots are not affected by those problems but face more challenges from the power density point of view. Prototypal machines were produced in the early 2010s. To name a few: StarlETH, with series elastic actuation; the MIT cheetah, based on quasi-direct drive. The lower technology readiness level (TLR), power density, and size can explain the gap with hydraulic robots. Despite their limitations, these robots showcased the potential of electric actuation, achieving energetically autonomous systems and efficient locomotion.

In a few years, these prototypes reached a higher TLR. MIT Cheetah 3 integrates additional DOFs and batteries to achieve 3D locomotion and untethered operations while maintaining a very low COT. HyQReal gave a suggestive demonstration by pulling a $3300\,\mathrm{Kg}$ aircraft [24] confirming the suitability of hydraulics for the most demanding use cases. Other research platforms showed higher payloads: IIT Centauro [25] and DFKI SpaceClimber [26] for example. However, this was achieved by using static gaits, lower velocities, or more legs. For these reasons, similar robots are not included in Tab I.

Several electric quadrupeds have been developed into commercial products, including Spot, Vision 60, and ANYmal. These robots incorporate multiple sensors to improve their locomotion performance and can operate autonomously for several kilometers. However, the level of robustness and integration achieved in these products comes at the cost of limited payload-to-mass ratios. The Unitree B1 and Jueying X20 are the only electric quadrupeds demonstrating a ratio higher than one, although not for continuous operations. Details on the design and control of these robots are not available.

Smaller robots show better payload-to-weight ratios. MIT Mini cheetah [27], SOLO [28], and Alphred [29] are good examples. The scaling laws of physics explain why the performance is so sensitive to the robot scale. Taking a reference length L, the mass scales proportionally to L^3, while gravity-induced joint torques scale according to L^4, because the mass-dependent contact forces are multiplied by the lever arm. The kinetic energy of rotating parts scales according to L^4 (assuming dynamic similarity), and the kinetic energy of the entire robot ranges between L^3 and L^5, depending on the assumptions on velocity [30]. The actuators' performance scale at a lower rate than the loads: torque density increases $\tau/M \propto L$, and motor constant $K_M \propto L^2$. This difference results in performance metrics, such as acceleration capability $\tau/J \propto L^{-1}$, to decrease [31] [32]. Moreover, both heat dissipation and characteristic time are proportional to L^2 [30]. As electric robots grow in size, they become overloaded by their own inertia, actuators become sluggish and inefficient, and the increased heat generated cannot be quickly dissipated and tends to concentrate in hot spots.

III. Design

We designed Barry to maximize the payload-to-weight ratio, limit energy consumption, and achieve fast, agile locomotion.

TABLE I: Overview of dynamically balancing quadruped robots' performance

Name	Type	Year	Leg size	Payload [kg]		Mass	Payload to	Velocity [m/s]		Power	Energy	Autonomy		COT
			[m]	Ref.	Max	[kg]	mass ratio[a]	Ref.	Max	[W]	[Wh]	[h]	[km]	
BigDog [9]	Hydr.	2008	1.1[a]	50	154	109	0.46-1.4	1.1	3.1	11000[b]	-	2.5	10	15[10]
HyQ [11]	Hydr.	2011	0.7	-	-	100	-	-	2	-	Offboard powered only			-
StarlETH [12]	Elec.	2012	0.4	-	25[c]	23	-	0.43	0.7	300	220	0.75	1.2	2.6
LS3 [13]	Hydr.	2012	1.0[a]	180	-	360	0.5	2.2	4.5	-	-	24	32	-
MIT cheetah [10]	Elec.	2013		-	-	33	-		4.5	380[d]	Offboard powered only			0.51[d]
HyQ2Max [14]	Hydr.	2015	0.7	40	-	80	0.5	-	-	-	Offboard powered only			-
ANYmal B [15]	Elec.	2017	0.6	15	-	30	0.3	0.8	1.6	290	580[a]	2.0	1.6[a]	1.2
MIT cheetah 3 [16]	Elec.	2018	0.68	-	235[c]	45	-	0.75	1.6	340[a]	450-900[b]	1.3[a]-2.0	1.0[a]	0.57-1.0[a]
HyQ2Real [17]	Hydr.	2019	0.74	-	-	130	-	-	-	-	-	-	-	-
Spot [6]	Elec.	2019	0.75[a]	14	-	32	0.44	-	1.6	376[a]	564	1.5	8.6[a]	0.73
Llama [18]	Elec.	2020	0.48	9	25[c]	67	0.13-0.37	0.75	1.7	3400[a]	1200	0.35[a]	0.27[a]	10
Jueying X20 [19]	Elec.	2021	0.75[a]	20	85	50	0.4-1.7	3.6	5.0	-	-	2-4	15	-
B1 [20]	Elec.	2021	0.75[a]	40	104	50	0.8-2.1	-	1.8	-	-	2-4	3.6-7.2[a]	-
VISION 60 [21]	Elec.	2021	0.68[a]	10	-	51	0.2	-	3	-	-	3.0[b]	10	-
ANYmal D [8]	Elec.	2021	0.66	15	-	50	0.3	0.75	1.3	530[a]	930	1.5-2	2-4	1.4[a]
Barry (this paper)	Elec.	2022	0.8	50	90	48	1.1-2	1.4	2.0	370	930	2.5[a]	9[a]	0.7

[a] Estimated from other parameters in this table or in the work cited. [b] Maximum value, not used for the estimation of other parameters. [c] Theoretical, from design specification or max joint torque, but not demonstrated in walking. Not used for the estimation of other parameters. [d] Not including power consumption due to computation.

IEEE Robotics and Automation Letters (RA-L) paper, presented at ICRA 2024, Yokohama, Japan. Cite as RA-L paper.

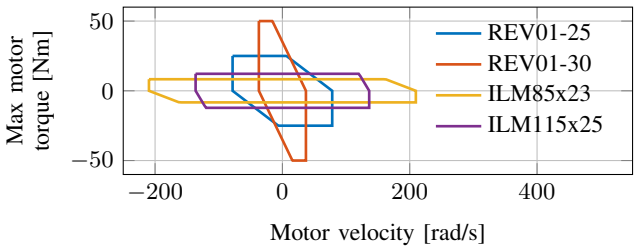

Fig. 2: Barry's motor exhibits torque-velocity limits dominated by the voltage constraint (sloped line). Comparable motors typically show a more typical behavior, where the maximum torque is mostly constrained by the magnets (flat region).

Moreover, we constrained ourselves to sealed solutions and protected designs to allow for outdoor operations and falls.

Barry uses the same main body of ANYmal and custom-designed legs and actuators. The robot weighs approximately $48\,\mathrm{kg}$ and has a hip height of $0.8\,\mathrm{m}$ at full leg extension, both the thigh and the shank are $0.4\,\mathrm{m}$ in length. The main body includes three computing units, a swappable LiPo battery, 4 realsense sensors (one per side), and two RGB cameras (one in the front and one in the back).

According to the analysis of Sec. II to optimise the robot's payload-to-weight ratio it is necessary to increase the actuators torque density, to maximise the spare torque available for payload, and manage their temperature, minimizing heat generation and increasing heat dissipation. To maintain a baseline, we chose to limit the robot's total mass to 50 kg, ANYmal's mass, resulting in a 2 kg mass budget per actuator.

The heat generated by actuators can be broken down into electronic losses, motor losses, and mechanical losses [10]. High-efficiency motor drivers can minimize electronic losses. We used custom motor drivers based on ANYdrive's design [15], which simplified integration with the main body. Motor losses can be further divided into components dominated by winding losses [34][35], especially at low velocities [36]. Winding losses P_{Elec}^{Losses} can be computed using Eq. 1, where τ stands for torque, N is the transmission ratio, and K_M is the motor constant.

$$P_{Elec}^{Losses} = \left(\frac{\tau_{Motor}}{K_M}\right)^2 = \left(\frac{\tau_{Joint}}{K_M N}\right)^2 \tag{1}$$

Mechanical losses P_{Mech}^{Losses} are caused by friction in the bearings and the transmission of the actuators. These losses can be modeled by the transmission efficiency η_T and are proportional to the mechanical power output of the joint, as shown in Eq. 2.

$$P_{Mech}^{Losses} = \frac{1-\eta_T}{\eta_T}|P_{Joint}^{Mech}| = \frac{1-\eta_T}{\eta_T}|\tau_{Joint}\omega_{Joint}| \tag{2}$$

TABLE II: Motor performance

Motor	Mass [kg]	τ_{Motor}^{Max} [Nm]	K_M [Nm/$\sqrt{\mathrm{W}}$]	N -	$K_M^2 N^2$ [Nm^2/W]
REV01-30	1.0	50	1.1	9.0	98.0
ILM115x25 [33]	1.1	13	0.87	5.33	21.5
LSI-160 [18]	2.1	43	0.64	5.25	11.3
HT05001 [10]	1.3	21	0.43	5.8	6.22
REV01-15	0.57	25	0.67	5.6	14.1
ILM85x23	0.62	8.3	0.48	14.4[a]	47.8[a]

[a] Theoretical

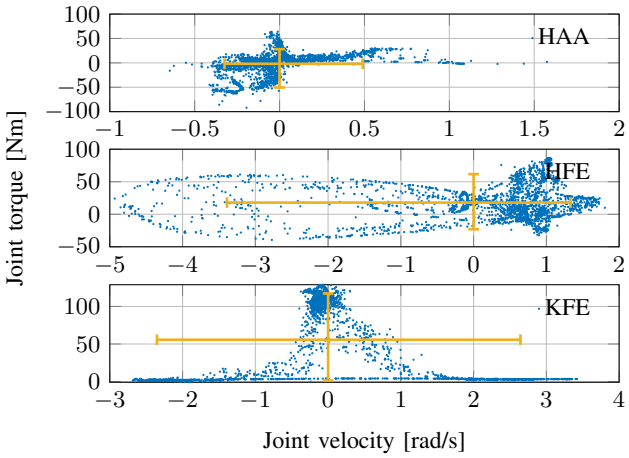

Fig. 3: Plot showing joint torque and velocity from the simulation of a $50\,\mathrm{kg}$ quadrupedal robot with $0.8\,\mathrm{m}$ long legs, trotting with $50\,\mathrm{Kg}$ of additional payload.

Despite being very simple models, Eq. 1 and 2 can be used to formulate a clear optimization goal: maximizing $K_M N$, while maintaining η_T sufficiently high to contain mechanical losses. The core design choices are the actuator selection and the motor-transmission pairing. We opted for quasi-direct drive architectures, which achieve high η_T with low N. This architecture helps increase torque density by eliminating the need for torque-sensing components and has low inertia.

To evaluate if motors could deliver the necessary torque and the ideal gear ratio, we used a simplified motor model and some reference torque-velocity trajectories. In Eq. 3 we considered both the magnets limit τ_{Motor}^{Max} and the voltage-limited torque, which affects torque output at higher velocities. The velocity constant K_V, torque constant K_T, electrical resistance R, and operating voltage V are the only parameters necessary for this model. Fig. 2 shows how Eq. 3 behaves differently for different motors: for some motors, the magnets limit torque τ_{Motor}^{Max} dominates the plot (horizontal line), while for others, the voltage-limited region (sloped line) is the dominating one.

$$\tau_{Motor} \leq \min\left\{\frac{K_T}{R}\left(-\frac{\omega_{Motor}}{K_V} + V\right), \tau_{Motor}^{Max}\right\} \tag{3}$$

We modeled Barry and tested its performance in simulation by adding up to $50\,\mathrm{kg}$ of additional payload. Figure 3 shows the joint-level torque-velocity trajectories used during the design phase. The knee joint experiences higher torques due to its coupling with the gravitational load.

To accommodate the different requirements we designed different actuators for the knee flexion/extension (KFE) the hip adduction/abduction and flexion/extension (HAA and HFE) joints. We selected REV01-30 for the knee joint because it allows a much higher $K_M^2 N^2$ value and peak torque than any other option, due to its design, optimized for high-torque and low-velocities regimes [37]. Table II shows how the selected

IEEE Robotics and Automation Letters (RA-L) paper, presented at ICRA 2024, Yokohama, Japan. Cite as RA-L paper.

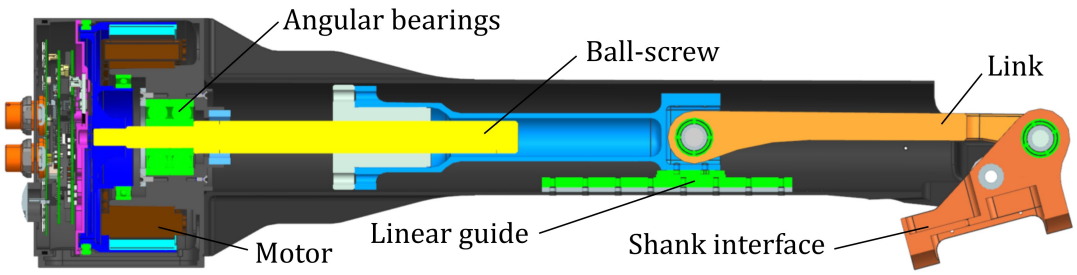

Fig. 4: Thigh and KFE actuator cross-section, showing the transmission to the knee, running coaxial to the structure.

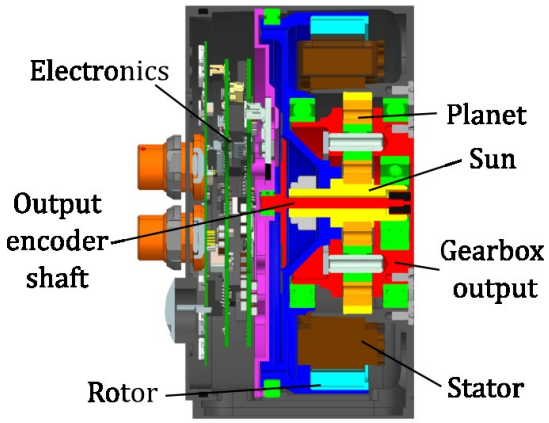

Fig. 5: Planetary actuator cross-section, showing the relative positioning of the motor, electronics, and gearbox. All bearings are shown in green.

motors compare to similarly sized motors in other robotic legs, with the last column highlighting the proportionality factor between the joint torque and the winding losses. The squared factor is a consequence of Eq. 1 and explains why small changes in design can explain big differences in the energetic performance. We selected a REV01-15 motor for the hip joints, which allows us to largely reuse the knee design. The ILM85x26 would theoretically allow for a better $K_M^2 N^2$, however, at the cost of a higher transmission ratio and a completely different design. Adjusting the motor windings would allow us to further optimize the design.

To produce the necessary reduction, we designed a custom single-stage planetary gearbox for the hip actuators, sized to withstand the motor's peak torque, a more challenging condition than the load of Fig. 3 and impact loads, without being limited by the gears. Moreover, we placed the planetary gearbox within the stator to increase compactness, resulting in an outer diameter of the ring gear of $60\,\mathrm{mm}$. This results in a transmission ratio of 5.6 (limited by sun gear strength), with 0.8 module gears, manufactured with 42CrMoS4 steel and induction hardened. To allow for load sharing between the

TABLE III: Barry's actuators specifications

	Peak torque [Nm]	Peak velocity [rad/s]	Mass [kg]	Idle power [W]
HAA/HFE	140	20	1.4	2.5
KFE fully folded	150	18	2.0	
KFE max GR	450	6.0	2.0	

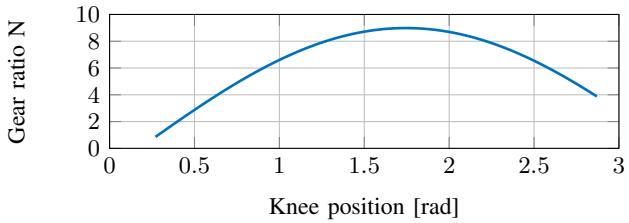

Fig. 6: Knee transmission ratio as a function of the knee angle. The knee angle is defined zero when the leg is straight.

teeth, we use 4 satellite gears which is possible because of the low N. The bearing structure is meant to transfer the bending moment (up to $200\,\mathrm{Nm}$) to the rotor bearing, decreasing the reaction forces and allowing for extremely thin bearings such as the KMF PBXU.

For the knee actuator, we used a high-pitch low-friction ball screw (THK SDA1520V) to achieve the reduction. The knee transmission ratio is limited by Eq. 3, and a higher reduction would result in insufficient maximum velocity. The knee actuator is almost identical to the planetary one, with angular contact bearing (supporting the axial load of the ball screw, up to $11\,\mathrm{kN}$) replacing the gearbox.

High-resolution 24-bit optical encoders are utilized for both the motor and output position, and an extra magnetic encoder is employed for initialization on the knee axis. EtherCAT is used for communication between the actuators and the main CPU. Tab. III lists the performance of the actuators, distinguishing between the gear ratio when the knee is fully folded and when is in around its maximum gear ratio. Even when the leg is fully folded, the knee actuator can produce more than enough torque to perform a stand-up maneuver. As visible in Fig 6, the fully extended leg results in an even lower gear ratio, however, this is less challenging because in that configuration the load produced by the robot's weight results in smaller knee torques.

The design of quadrupedal robot legs is based on maximizing the range of motion and minimizing inertia. This has led to the convergent evolution of 3 DOF articulated systems with a transmission to the knee. Barry follows this design, with its three actuators serially connected as shown in Fig. 4. This configuration minimizes the antagonistic work associated with closed chain kinematics [38], and the knee transmission reduces inertia. The legs' joints are arranged in HAA-HFE-KFE sequence, with all the knees pointing backward to avoid self-conflict due to link lengths. The low inertia enables fast correction steps, improves stability, and reduces the required hip actuators' torque.

IEEE Robotics and Automation Letters (RA-L) paper, presented at ICRA 2024, Yokohama, Japan. Cite as RA-L paper.

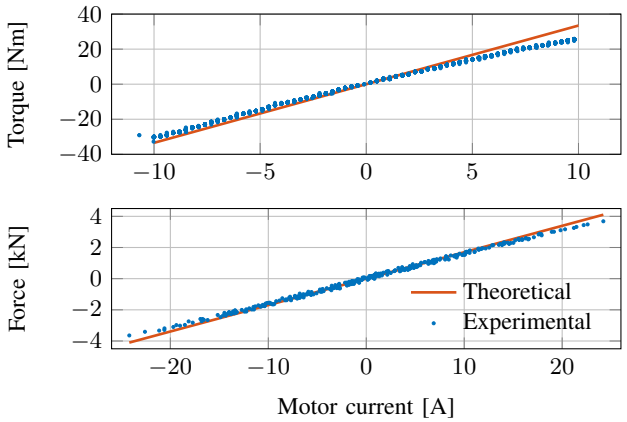

Fig. 7: Experimental characterization of the planetary gearbox and ball screw actuators compared with the expected theoretical behaviors.

The motion of the knee is transmitted through a linkage, as shown in Fig. 4, with a linear rail providing guidance and reacting to off-axis loads. The linkage lever's effective length changes throughout the knee's range of motion, resulting in a variable gear ratio, shown in Fig. 6. The knee's range of motion is limited to $150°$. A more sophisticated linkage would allow for extending the range of motion and optimizing the gear ratio curve [14]. However, we chose a single-link solution for its efficiency and stiffness. The linkage is designed to have the peak gear ratio at $\theta_{KFE} = 100°$, maximizing the gear ratio in the most frequently used region of the range of motion.

The ball screw is coaxial with the thigh, which is a single machined aluminum part that also serves as a heat sink for the knee actuator. A clamp is driven by the linkage and holds an aluminum tube, where a rubber foot is attached. The total weight of the leg structure, transmission, and bearings without the KFE actuator is only $1.4\,\mathrm{kg}$.

IV. Software Architecture and Locomotion Controller

The software architecture of Barry is based on the one of ANYmal. The main component is a high-level controller commanding the joints to produce the desired robot motion. A state estimator fuses the robot's various sensors to estimate quantities required by the high-level controller. A low-level controller handles the communication with the actuators. We keep the low-level controller and state estimator mostly unchanged from [15] but develop a high-level controller based on a neural network trained with deep reinforcement learning.

The high-level policy is trained in simulation following the approach proposed in [39], which we adapted to Barry's kinematic and dynamic properties. In our training environment, we included a simplified model of the actuators that accounts for the torque limits as a function of motor velocity, as shown in Fig. 2. Since the knee actuators' torque limits also depend on joint position, we incorporated the gear ratio into the model. Unlike the approach in [40], we did not train a neural network-based actuator model.

The policy output is interpreted as desired joint positions θ^*_{Joint}, which are then transformed into desired joint torques τ^*_{Joint} by an ideal PD controller. Finally, desired joint torques

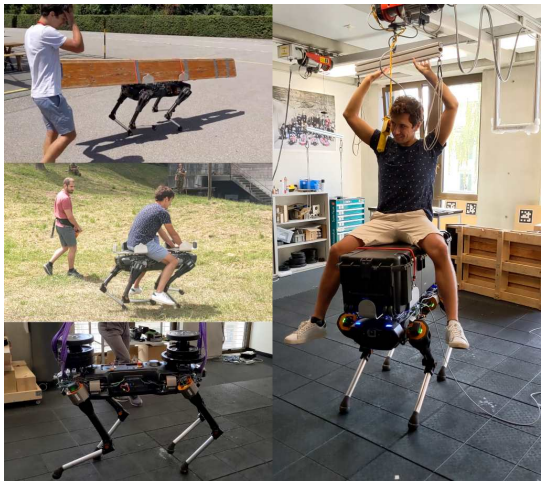

Fig. 8: These images show Barry carrying different unmodeled payloads: two wooden benches, a person, gym weights, and a $70\,\mathrm{kg}$ person on top of a $20\,\mathrm{kg}$ box.

are clipped to the possible range defined in Eq. 3, and the resulting possible torques τ_{Motor} are sent to the simulation. The following equations summarize the process:

$$\begin{aligned} \tau^*_{Joint} &= P(\theta^*_{Joint} - \theta_{Joint}) - D\omega_{Joint} \\ \tau^*_{Motor} &= \tau^*_{Joint}/N(\theta_{Joint}) \\ \omega_{Motor} &= \omega_{Joint}N(\theta_{Joint}) \\ \tau_{Motor} &= \min(\max(\tau^*_{Motor}, \check{\tau}_{Motor}), \hat{\tau}_{Motor}) \end{aligned} \tag{4}$$

where $\hat{\tau}_{Motor}$ and $\check{\tau}_{Motor}$ are the right side of Eq. 3 for positive and negative motor velocities. To encourage the policy to stay within the actuator limits, we introduce penalties for violating the torque and velocity limits.

$$\begin{aligned} r_{\tau-limit} &= \max(||\tau_{Motor}|| - \tau^{Max}_{Motor}, 0)^2 \\ r_{\omega-limit} &= \max(||\omega_{Motor}|| - \omega^{Max}_{Motor}, 0)^2 \end{aligned} \tag{5}$$

Furthermore, as the gear ratio varies, minimizing τ_{Motor} does not correspond to minimizing τ_{Joint}. Therefore, we incorporate τ_{Motor} in the torque penalty calculation.

In order to prevent damage due to mechanical limits, the policy is trained to stay within Barry's knee joint range by introducing a penalty for violating joint limits.

$$\begin{aligned} r_{\theta-limit} = \min(\theta_{Joint} * Max - \theta_{Joint}, 0) + \\ + \min(\theta_{Joint} - \theta_{Joint} * Min, 0) \end{aligned} \tag{6}$$

$\theta_{Joint} * Max$ and $\theta_{Joint} * Min$ are defined as 95% of the actual mechanical limits.

To prepare the policy for high payloads, we randomize the weight of the robot's base during training by adding up to 100kg. We find that the policy is able to adapt to a wide range of weights without any additional information about the mass.

V. Experiments and Results

To validate the performance of the newly developed actuators, we conducted experimental characterization by connecting the output of the actuators (the moving nut for the linear drive) to a commercial six-axis force/torque sensor (BotaSys MegaONE) and commanding arbitrary motor currents. Fig. 7 shows that the measured torque and axial force are consistent with those estimated using the motors' current and

IEEE Robotics and Automation Letters (RA-L) paper, presented at ICRA 2024, Yokohama, Japan. Cite as RA-L paper.

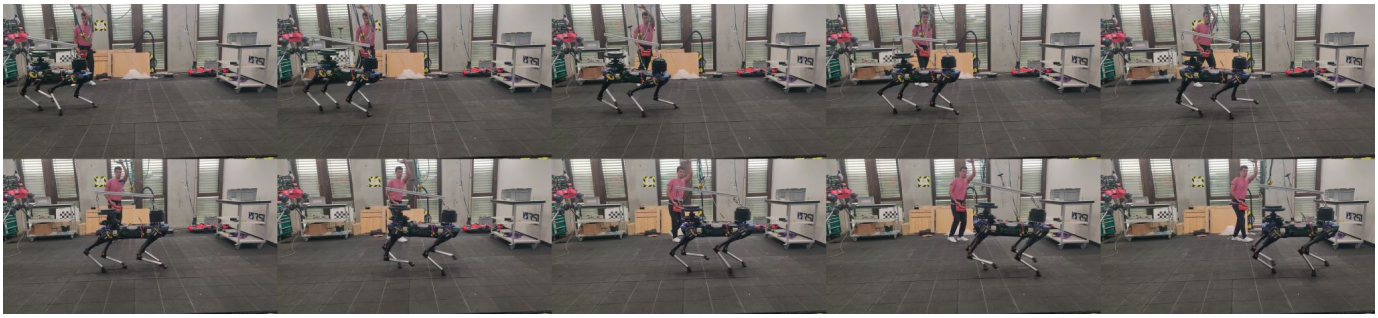

Fig. 9: A sequence of frames from a video showing Barry carrying a 66 kg dummy payload on top of the main body.

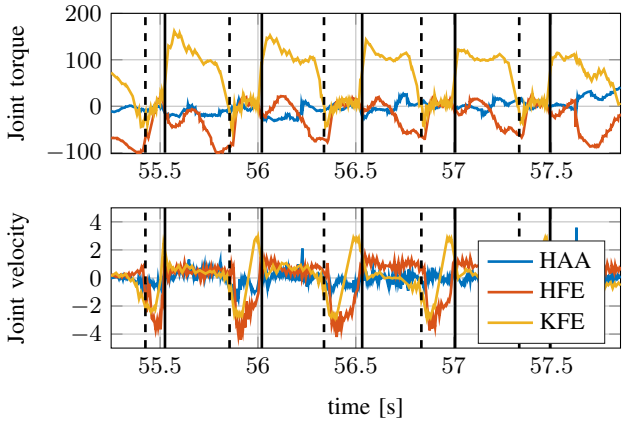

Fig. 10: Joint torques and velocities during the experiment of Fig. 9, the solid black lines represent touchdown, the dashed ones liftoff. These plots are representative of the actuators' load when the robot walks at a steady velocity of $0.6\,\mathrm{m/s}$

torque constant. However, some data dispersion and deviation from linearity are visible in the plot. These anomalies can be explained by various effects such as friction, stick-slip, hysteresis, and field saturation.

To test Barry's strength and its controller effectiveness, we loaded it with dummy payloads consisting of gym weights. As mentioned in IV, we do not model the inertia properties of the payload. Fig. 9 shows Barry performing a dynamic walk in the lab with a 66 kg dummy payload, while Fig. 8 shows some additional payload tests. We tested up to 90 Kg payload, successfully taking a few steps at low velocities without experiencing thermal failures. With big payload masses, the higher center of mass has a destabilizing effect, which results in more corrective steps and a higher failure rate. Fig. 10 shows the torque and velocities for one leg's joints while walking with such additional mass. In all these experiments there was no sign of instability or struggle because of the unmodeled inertia.

In Fig. 13, the joint efforts are compared with the loads derived from simulations in III. It is noticeable how close the distributions are and their location compared to the actuator limits. A payload mass of 50 kg was used, which was also used in the design phase. The only significant difference between the simulation and experimental data is observed in the HFE torque. The positioning of the knee actuator explains the discrepancy. The design is lighter than what was assumed in the simulation phase, which reduces the inertial loads on the HFE joint, thereby affecting the mean torque.

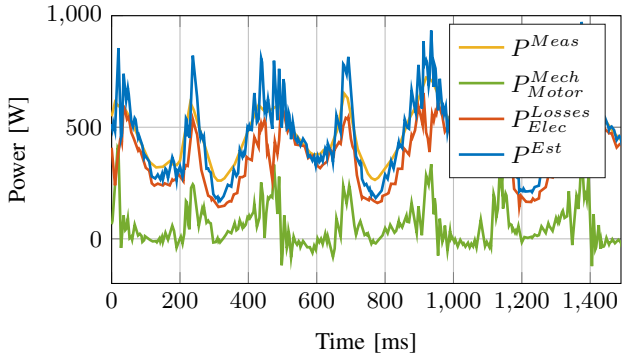

Fig. 11: Total measured power consumption $P^{Meas}$of the robot compared with winding losses P^{Losses}_{Ele}, mechanical output P^{Mech}_{Motor}, and estimated power consumption P^{Est} according to Eq. 7. Acquired while carrying 6 kg, and tracking a variety of velocity commands.

We measured the total power consumption of Barry using an external calibrated bidirectional power supply, EPS 9200-140 3U, rated for 10 kW. The measurements were done with the battery still installed but electrically disconnected and included the consumption of the main body's components and of the actuators. The total power consumption during one of the walking experiments is shown in Fig. 11, which includes 41 W idle power consumption. We use the readings from the actuators and the idle power consumption to estimate the total power consumption. We compute the winding losses caused by the torque production and the joint mechanical power as shown in Eq. 7. The estimation of the mechanical power is not affected by the mechanical losses of the transmission, as it happens at the motor level. Fig. 11 shows also winding losses, mechanical power and estimated power consumption.

$$\begin{aligned} P^{Est} &= P^{Idle} + P^{Losses}_{Elec} + P^{Mech}_{Motor} \\ &= P^{Idle} + \sum_{i=1}^{12} \left(\frac{\tau^i_{Motor}}{K_M} \right)^2 + \sum_{i=1}^{12} \tau^i_{Motor} \omega^i_{Motor} \end{aligned} \tag{7}$$

To validate the accuracy of this estimation method, we loaded Barry with dummy masses and commanded various motions for a few minutes. We used the same setup described above to log the total power consumption. Fig 12 shows the mean, standard deviation, min and max values for both the measured and the estimated power consumption. The mean value of the estimated power consumption differs by ±3%, which we consider acceptable for the scope of our work. Estimated minimal and maximal values are affected by a more

IEEE Robotics and Automation Letters (RA-L) paper, presented at ICRA 2024, Yokohama, Japan. Cite as RA-L paper.

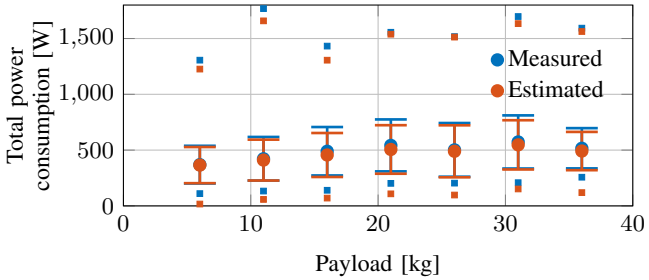

Fig. 12: Barry's total power consumption was measured with different additional masses while tracking a variety of velocity commands. The measured values are represented in blue, and the estimated values are represented in red according to Eq. 7. The round markers represent the average value, and the squared markers represent the maximum and minimum values. The vertical bars represent one standard deviation of the measured power consumption for each experiment. There is no data point at 0 because the payload interface weighs 6 kg.

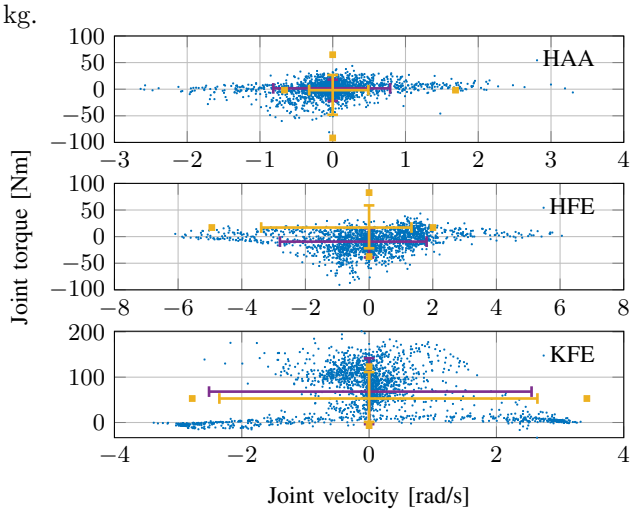

Fig. 13: Plot showing joint torque and velocity logged from an experiment with 50 kg payload. The purple bars define the region that contains the central 90% of the torque and velocity distributions, and they cross each other at the mean value of torque and velocity. The yellow lines have the same meaning but for the simulated dataset of Fig. 3 and are added for comparison. The yellow squares represent the extreme values of the simulated distribution of torque and velocities.

significant error, but they are not used for derived metrics such as the COT.

To further characterize Barry's energetic performance, we estimated the COT using Eq. 8, where v represents the base velocity and g represents the gravity acceleration. The total power consumption P^{Est} and the total mass (robot and payload) m_{Tot} were used as inputs to the equation.

$$COT = \frac{P^{Est}}{vgm_{Tot}} \tag{8}$$

To minimize the impact of uneven velocities and accelerations, we conducted the experiment by commanding Barry to move at maximum longitudinal velocity for approximately 10 m, repeating the experiment several times. We recorded the data, computed the total energy consumption using the method

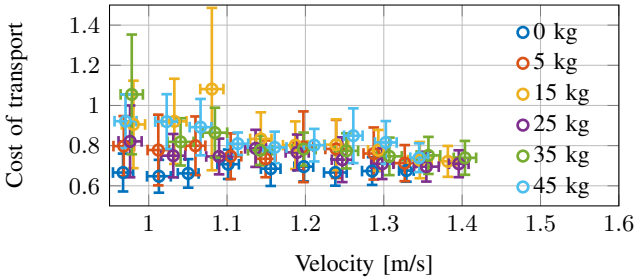

Fig. 14: Plot showing Barry's COT at different walking velocities, with different colors representing data acquired with different dummy payload masses. The error bars indicate the variance of the measurements at each velocity.

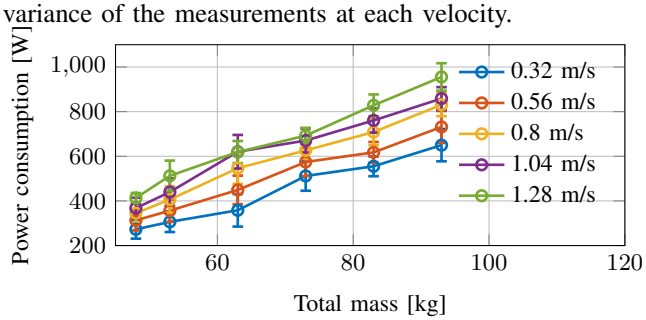

Fig. 15: Plot showing the relationship between total power consumption (averaged over one stride) and total mass (sum of robot mass and dummy payload). The lines represent the power consumption at different velocities, while the error bars represent the standard deviation of the measures.

described above, and used the state estimator to evaluate the robot's linear velocity. We then computed the COT, discarding values below 0.9 m/s to minimize border effects and artifacts due to accelerations. Finally, we repeated the experiment with different payload masses to evaluate the impact on the COT.

Fig. 14 depicts the COT as a function of walking velocity. The error bars for experiments with different payloads largely overlap, indicating that the COT does not depend strongly on payload mass. Figs. 15 and 16 provide further insight into how power consumption varies with payload mass and walking velocity. The experimental data indicate a linear relationship between power consumption and total robot mass, which is consistent across all walking velocities; see Fig. 15. Additionally, there is an almost linear relationship between walking velocity and power consumption, which holds across all experiments performed with various payload masses.

VI. Conclusion

This paper introduces a new legged robot platform named Barry. We present the detailed design considerations, engineering trade-offs, and sizing processes that lead to a configuration with superior performance compared to existing quadrupeds. Theoretical considerations are used to derive design criteria, which outcome is compared to other state-of-the-art designs. The torque-dense actuators allow for high payloads while being energy efficient and capable of dynamic locomotion. The neural network-based controller can handle the nonlinearities of the design and unmodeled payloads with masses even larger than the robot itself. The controller's robustness against inertia properties greatly simplifies the robot's usage, as no

IEEE Robotics and Automation Letters (RA-L) paper, presented at ICRA 2024, Yokohama, Japan. Cite as RA-L paper.

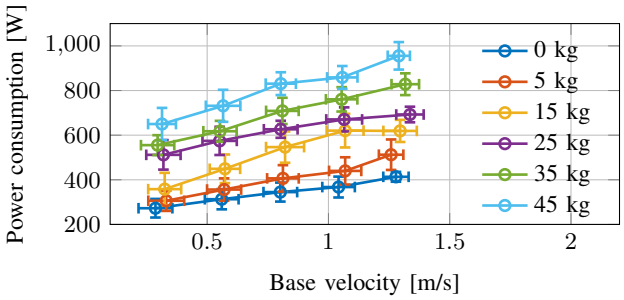

Fig. 16: The plot shows the relationship between the total power consumption, averaged over one stride, and the robot velocity. The different lines represent the power consumption with different dummy payload masses, as explained by the legend. The error bars represent the standard deviation of the measurements.

robot model adjustment or parameter tuning is necessary when changing the payload. Extensive testing experiments are presented to validate the design assumptions and characterize Barry's performance.

All of these developments are aimed at investigating the feasibility of using walking robots as transportation machines. With its integration of all these features, Barry successfully demonstrates the possibility of practical transportation robots.

In the future, we will keep developing Barry under multiple aspects. We plan to fully integrate perception in the locomotion controller to overcome terrains and obstacles that are currently infeasible. We want to leverage hardware and software synergies to understand and reduce energy consumption further. Finally, we aim to integrate payloads too massive for available quadrupedal robots and showcase possible applications. Given Barry's efficiency and extensive payload capabilities, we are exploring applications that require high endurance, such as day-long field missions.

REFERENCES

[1] "Atlas™." [Online]. Available: https://www.bostondynamics.com/atlas

[2] [Online]. Available: https://www.darpa.mil/program/darpa-robotics-challenge

[3] M. Tranzatto, "Cerberus: Autonomous legged and aerial robotic exploration in the tunnel and urban circuits of the darpa subterranean challenge," *Journal of field robotics.*, 2021.

[4] A. Bouman *et al.*, "Autonomous spot: Long-range autonomous exploration of extreme environments with legged locomotion," in *2020 IEEE/RSJ International Conference on Intelligent Robots and Systems (IROS)*. IEEE, 2020, pp. 2518–2525.

[5] I. D. Miller *et al.*, "Mine tunnel exploration using multiple quadrupedal robots," *IEEE Robotics and Automation Letters*, vol. 5, no. 2, pp. 2840–2847, 2020.

[6] "Spot." [Online]. Available: https://www.bostondynamics.com/spot

[7] "Aliengo." [Online]. Available: https://www.unitree.com/

[8] "Anymal - autonomous legged robot," May 2021. [Online]. Available: https://www.anybotics.com/anymal-autonomous-legged-robot/

[9] M. Raibert *et al.*, "Bigdog, the rough-terrain quadruped robot," *IFAC Proceedings Volumes*, vol. 41, no. 2, pp. 10 822–10 825, 2008, 17th IFAC World Congress.

[10] S. Seok *et al.*, "Design principles for highly efficient quadrupeds and implementation on the mit cheetah robot," in *2013 IEEE International Conference on Robotics and Automation*, 2013, pp. 3307–3312.

[11] C. Semini *et al.*, "Design of hyq – a hydraulically and electrically actuated quadruped robot," *Proceedings of the Institution of Mechanical Engineers, Part I: Journal of Systems and Control Engineering*, vol. 225, no. 6, pp. 831–849, 2011.

[12] M. Hutter, "Starleth & co.: Design and control of legged robots with compliant actuation," Ph.D. dissertation, ETH Zurich, 2013.

[13] BostonDynamics, "Ls3 - legged squad support system," Sep 2012. [Online]. Available: https://youtu.be/R7ezXBEBE6U

[14] C. Semini *et al.*, "Design of the hydraulically actuated, torque-controlled quadruped robot hyq2max," *IEEE/ASME Transactions on Mechatronics*, vol. 22, no. 2, pp. 635–646, 2017.

[15] M. Hutter *et al.*, "Anymal - toward legged robots for harsh environments," *Advanced Robotics*, vol. 31, no. 17, pp. 918–931, 2017.

[16] G. Bledt *et al.*, "Mit cheetah 3: Design and control of a robust, dynamic quadruped robot," in *2018 IEEE/RSJ International Conference on Intelligent Robots and Systems (IROS)*. IEEE, 2018, pp. 2245–2252.

[17] C. Semini *et al.*, "Brief introduction to the quadruped robot hyqreal," *Istituto di Robotica e Macchine Intelligenti (I-RIM)*, 2019.

[18] J. Nicholson *et al.*, "Llama: Design and control of an omnidirectional human mission scale quadrupedal robot," in *2020 IEEE/RSJ International Conference on Intelligent Robots and Systems (IROS)*. IEEE, 2020, pp. 3951–3958.

[19] D. Robotics, "Jueying x20." [Online]. Available: https://www.deeprobotics.cn/en/products_jy_303.html

[20] *Unitree B1: Super load capacity, super protection level, go anywhere.* Unitree, Jun 2022. [Online]. Available: https://youtu.be/wSOlpth8FaE

[21] "Vision 60: Ghost robotics." [Online]. Available: https://www.ghostrobotics.io/vision-60

[22] C. Semini, "Hyq-design and development of a hydraulically actuated quadruped robot," *Doctor of Philosophy (Ph. D.), University of Genoa, Italy*, 2010.

[23] "Inside the lab: How does atlas work?" Aug 2021. [Online]. Available: https://youtu.be/EezdinoG4mk?t=120

[24] *HyQReal robot release: Walking robot pulls a plane (extended version).* IIT, May 2019. [Online]. Available: https://youtu.be/pLsNs1ZS_TI

[25] N. Kashiri *et al.*, "Centauro: A hybrid locomotion and high power resilient manipulation platform," *IEEE Robotics and Automation Letters*, vol. 4, no. 2, pp. 1595–1602, 2019.

[26] S. Bartsch *et al.*, "Development of the six-legged walking and climbing robot spaceclimber," *Journal of Field Robotics*, vol. 29, no. 3, pp. 506–532, 2012.

[27] B. K. et al., "Mini cheetah: A platform for pushing the limits of dynamic quadruped control," in *2019 International Conference on Robotics and Automation (ICRA)*, May 2019, pp. 6295–6301.

[28] F. Grimminger *et al.*, "An open torque-controlled modular robot architecture for legged locomotion research," *IEEE Robotics and Automation Letters*, vol. 5, no. 2, pp. 3650–3657, 2020.

[29] J. Hooks *et al.*, "Alphred: A multi-modal operations quadruped robot for package delivery applications," *IEEE Robotics and Automation Letters*, vol. 5, no. 4, pp. 5409–5416, 2020.

[30] M. Wautelet, "Scaling laws in the macro-, micro- and nanoworlds," *European Journal of Physics*, vol. 22, no. 6, pp. 601–611, oct 2001.

[31] P. M. Wensing *et al.*, "Proprioceptive actuator design in the mit cheetah: Impact mitigation and high-bandwidth physical interaction for dynamic legged robots," *Ieee transactions on robotics*, vol. 33, no. 3, pp. 509–522, 2017.

[32] K. J. Waldron *et al.*, "Scaling of robotic mechanisms," in *Proceedings 2000 ICRA. Millennium Conference. IEEE International Conference on Robotics and Automation. Symposia Proceedings (Cat. No. 00CH37065)*, vol. 1. IEEE, 2000, pp. 40–45.

[33] J. Hwangbo *et al.*, "Cable-driven actuation for highly dynamic robotic systems," in *2018 IEEE/RSJ International Conference on Intelligent Robots and Systems (IROS)*, 2018, pp. 8543–8550.

[34] S. Seok *et al.*, "Design principles for energy-efficient legged locomotion and implementation on the mit cheetah robot," *IEEE/ASME Transactions on Mechatronics*, vol. 20, no. 3, pp. 1117–1129, 2015.

[35] T. Zhu *et al.*, "Design, modeling, and analysis of a liquid cooled proprioceptive actuator for legged robots," in *2019 IEEE/ASME International Conference on Advanced Intelligent Mechatronics (AIM)*, 2019, pp. 36–43.

[36] M. Budinger *et al.*, "Estimation models for the preliminary design of electromechanical actuators," *Proceedings of the Institution of Mechanical Engineers, Part G: Journal of Aerospace Engineering*, vol. 226, no. 3, pp. 243–259, 2012.

[37] P. Nguyen *et al.*, "Human-like direct drive robot," May 2 2017, cA3052893A1.

[38] A. M. Abate, "Mechanical design for robot locomotion," 2018.

[39] N. Rudin *et al.*, "Learning to walk in minutes using massively parallel deep reinforcement learning," in *Conference on Robot Learning*. PMLR, 2022, pp. 91–100.

[40] J. Hwangbo *et al.*, "Learning agile and dynamic motor skills for legged robots," *Science Robotics*, vol. 4, no. 26, p. eaau5872, 2019.